RESEARCH ARTICLE

Schlieren diagnostic for cinematic visualization of dense plasma jets at Alfvénic timescales

Thomas C. Underwood[1] · **Keith T. K. Loebner[1]** · **Victor A. Miller[2]** · **Mark A. Cappelli[1]**

Abstract
The manner in which magnetized plasma jets evolve remains key to better understanding the behavior of hydromagnetic systems and providing new insights into how they can be dynamically controlled. In this work, we present the underlying theory, apparatus, and optical features of a schlieren diagnostic capable of cinematically visualizing dense plasma jets. We identify the range of plasma density over which the diagnostic is sensitive and describe ways to further improve image contrast. This diagnostic features the unique ability to simultaneously resolve both the characteristic Alfvénic timescales and spatial flow features with continuous acquisition over the lifetime of a jet. We use this diagnostic to visualize the formation and evolution of hydromagnetic jets produced from a plasma gun device. Dynamic coherent flow features are identified and tracked over time throughout the evolutionary progression of plasma jets. Finally, the process by which these coherent features translate into perturbations of magnetized bow shocks is visualized.
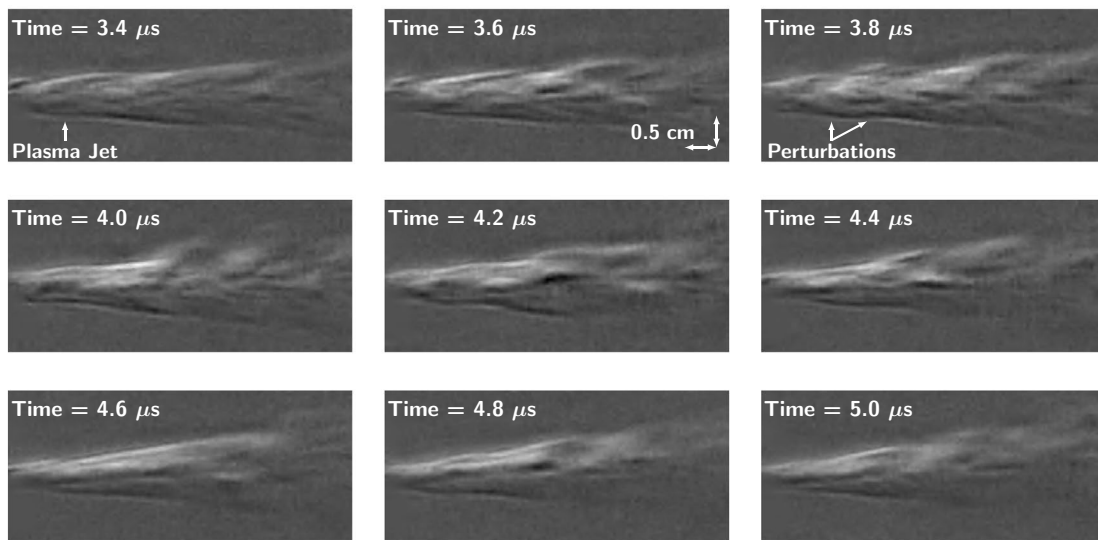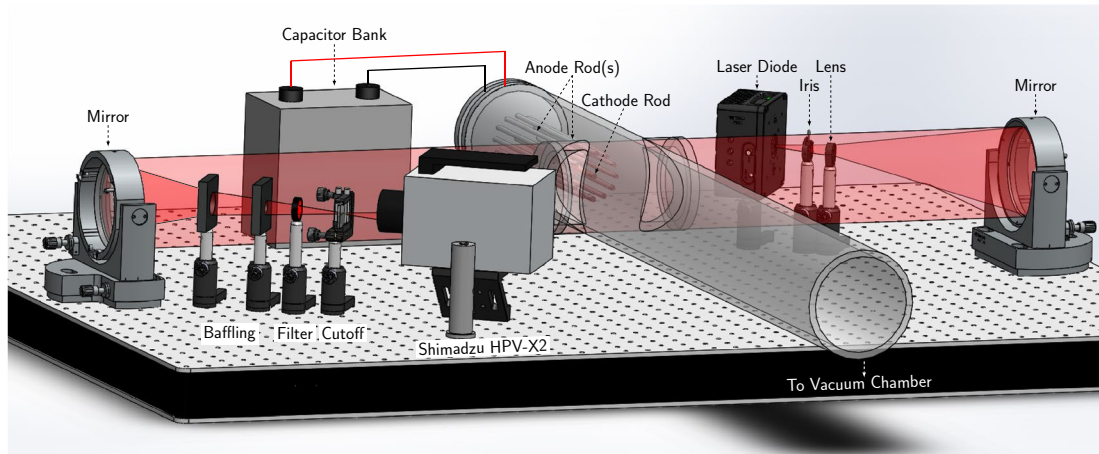
✉ Thomas C. Underwood
  tcunderwood1@gmail.com

[1] Department of Mechanical Engineering, Stanford University, Stanford, CA 94305, USA

[2] SeekOps, Inc., Austin, TX 78745, USA

Graphical abstract

Experimental schematic of the schlieren apparatus and plasma source used in this study. A z-type schlieren conﬁguration is used with a 630 nm, 250 mW laser backlight source, two *f*/4 60 cm focal length mirrors, and a 'sooted' slide as an optical cutoff. Flow dynamics are captured with a Shimadzu HPV-X2 with a continuous sample rate of 10 MHz. The source used to produce hydromagnetic plasma jets is a gun device. The development of coherent flow structures is observed indicating that the transition to quasi-steady flow is a dynamic process

1 Introduction

With the advent of modern high-speed imaging systems, it is now becoming possible to visualize both the structure and dynamics of previously inaccessible phenomena. Such visualization have contributed to breakthroughs in fields ranging from erosion (Hassani-Gangaraj et al. 2018) to biology (Patek and Caldwell 2005) and have proven essential in better understanding the underlying physics that govern them. Similar opportunities exist to expand the knowledge of both hypersonic and plasma flows where conventional visualization approaches have been unable to resolve the widely disparate temporal and spatial scales over prolonged periods. Among these, hydromagnetic plasma jets in particular offer exciting research opportunities with applications including astrophysics (Underwood et al. 2017), plasma jet driven magneto-inertial fusion (PJMIF) (Thio 2008; Cassibry et al. 2006, 2009), z-pinches schemes (Bickerton 1980; Shumlak et al. 2001), and space propulsion (Cheng 1970). Detailed knowledge of the plasma's evolution in structure and stability have important implications for both fundamental and laboratory-scale systems. However, visualizing the evolution of such systems is a difficult task as it requires diagnostics

to simultaneously resolve both the flow features and the characteristic scales over which perturbations grow.

Techniques that rely on changes in the refractive index of a medium to either modify recorded levels of background illumination or cause interference have been used extensively to visualize transparent flows. Schlieren imaging is a refractometric technique that visualizes gradients in the refractive index of an inhomogeneous medium as gradients in the recorded intensity of background light that propagates through it (Settles 2012; Merzkirch 2012). A major advantage of this diagnostic is its ability to tune both the sensitivity and measurement range to visualize desired flow features by adjusting the amount of refracted light cutoff in the optical path. Such features have made schlieren techniques standard in visualizing compressible flow phenomena such as shocks where large gradients in neutral density can be easily captured with a tunable sensitivity that matches the expected flow conditions. Schlieren has also been used to visualize plasma where both electrons and ions contribute to changes in the refractive index of the flow. Hydromagnetic plasma jets in particular overcome many of the challenges with interpreting species-specific flow features that are present in partially ionized gases due to their high characteristic temperatures and densities.

Although schlieren methods have been used previously to study plasmas (Nakajima et al. 2015; Kalantar and Hammer 1993), there are noticeable gaps in literature regarding both the underlying theory and the added features necessary to overcome the complexities associated with plasma flows. Beyond that, there is a need to develop a diagnostic capable of simultaneously resolving both the temporal and spatial scales of plasma jets throughout their evolution. In this paper, we present a novel schlieren apparatus that is capable of simultaneously resolving these scales and use it to cinematically visualize the evolution of a quasi-stationary z-pinch. Unlike conventional studies that rely on single images and assume experimental repeatability, we visualize dynamic changes in the jet structure all in one discharge event as the driving current profile changes. Detailed descriptions of the underlying theory and customized optical features of the diagnostic are included to detail how both the sensitivity and contrast can be improved. The diagnostic is compared to cinematic measurements of broadband emission to illustrate the added flexibility and improved sensitivity that schlieren methods offer. Finally, the platform is used to delineate the unsteady features of bow shock formation around magnetized bodies such as Earth.

2 Theory

As light rays propagate through an inhomogeneous medium, changes in the index of refraction, N, cause the speed of light, $v = c/N$, to change and in response, the light to bend over its path length. In neutral gases specifically, the propagating light locally distorts the charge configuration of gas molecules and induces dipole moments that cause the light's refraction. When the index of refraction is close to unity in neutral gases, its refractivity, $N - 1$, is proportional to its density, ρ, and the characteristic Gladstone–Dale coefficient which depends on both the wavelength of light and the properties of the medium it is traversing (Gladstone and Dale 1863). As temperature rises in gases, the fractional population of both free electrons and ions begin to significantly contribute to the refractivity of the medium. For a medium with an arbitrary level of ionization, the refractivity can be expressed according to,

$$N - 1 = \rho\left[\alpha_I K_I + \alpha_D K_A + (1 - \alpha_I - \alpha_D)K_M\right] \cdots \\ + K'_e(n_e, B), \tag{1}$$

where K_I, K_A, and K_M are the Gladstone-Dale coefficients due to ions, atoms, and molecules, respectively. Of the remaining terms, α_I and α_D are the mass fractions of ions and atoms in the gas mixture, respectively. The remaining term, $K'_e(n_e, B)$, describes the contributions that free electrons play on the refractivity of the gas mixture. As detailed in Appendix, the general propagation of an electromagnetic wave into a nonthermal hydromagnetic plasma depends on the electron density, magnetic field, and angle between the direction of wave propagation and the ambient magnetic field.

Given that the refractivity of a gas mixture depends strongly on its composition, it is useful to quantify the relative contribution of atomic, molecular, and plasma species as a function of temperature. To do this, a set of equations describing the balance between dissociation, ionization, and recombination, and thus the densities, n, of each species must first be written. Specifically, using the law of mass action for hydrogen, the experimental working gas considered in this work, the equations can be written as,

$$\frac{n_e n_H^+}{n_H} = \frac{1}{V}\frac{Q_e Q_H^+}{Q_H}\exp\left(-\frac{\epsilon_I}{k_B T}\right), \tag{2}$$

$$\frac{n_H^2}{n_{H_2}} = \frac{1}{V}\frac{Q_H^2}{Q_{H_2}}\exp\left(-\frac{\epsilon_D}{k_B T}\right), \tag{3}$$

where ϵ_I and ϵ_D are the ionization and dissociation energy of H and H_2, respectively. Expressions for each component of the various species partition functions, Q, can be found in textbooks covering statistical thermodynamics (Mitchner and Kruger 1992).

The result of this calculation is shown in Fig. 1a for a prescribed density of H_2 at room temperature (5×10^{22} m^{-3}). As the equilibrium temperature of the mixture increases, H_2 dissociates to atomic hydrogen. Eventually near $T \sim 10^4$ K, the

atomic hydrogen begins to ionize and beyond $T \sim 3 \times 10^4$ K, the mixture become fully ionized in equilibrium conditions. Clearly for high temperature plasmas, the refractivity is dominated by ions and free electrons as all of the atomic and molecular species have been ionized.

The evaluation of refractivity detailed in Eq. 1 also requires knowledge of the Gladstone-Dale coefficients for H_2, H, and H^+, respectively, as a function of both wavelength and mixture temperature. Both K_H and K_{H_2} have been measured experimentally at prescribed temperatures and are tabulated in physical chemistry and gas dynamic references (White 1961; Merzkirch 2012). Experimental measurements for K_{H+}, however, are severely limited and approximate calculation methods based on computed polarizability are typically employed (Alpher and White 1959). To evaluate the free electron contribution, we assume a parallel wave propagation relative to magnetic field lines, $\theta = 0$, and

(a)

(b)

Fig. 1 Plot of species specific **a** number density and **b** refractivity as a function of equilibrium temperature. In this treatment, it is assumed magnetic effects are negligible and $\lambda = 630$ nm

further that $\omega_H/\omega \ll 1$ where $\omega_H = B_0|e|/m_e$ is the electron cyclotron frequency and ω is the optical angular frequency of the background light source. Invoking these assumptions and further assuming $n_e \ll n_c$ (cutoff density) $= \omega^2 m_e \epsilon_0/e^2$ then $K'_e(n_e, B) \approx -n_e/2n_c$ and is independent of the local magnetic field strength. As we will show in proceeding sections, these assumptions approximate schlieren visualization of magnetized plasma jets as gradients in magnetic field strength contribute negligibly to recorded signals compared to gradients in plasma density.

The results of the refractivity calculation for the gas mixture is detailed in Fig. 1b and includes the equilibrium species densities shown in Fig. 1a. In this work, consistent with most laboratory plasma jets, we focus on the temperature regime $T \gg 10^4$ K where the refractivity is dominated by contributions from free electrons. At any given wavelength, the contribution to the mixture refractivity per electron is both negative and over an order of magnitude higher than the contribution per neutral particle.

In schlieren systems, deflections in background light sources are marked by relative changes in illumination or color. By invoking geometrical theory, the variation in image illumination, I, induced by refractive effects can be expressed in terms of the variation in recorded light transmission, t. The contrast of schlieren images, or the ratio of differential to background illumination, can be expressed as $\Delta I/I_0 = \Delta t/t_0$. In accordance with the presentation by Merzkirch (2012), the variation in the measured light transmission can also be expressed directly in terms of the refraction angle, ϵ, experienced by light rays propagating through a test section, $\Delta I/I_0 \sim \epsilon$. By further assuming the refraction angles are small, $\tan \epsilon \sim \epsilon$, the schlieren contrast can be expressed as as a function of the gradient of the refractive index detailed in Eq. 1,

$$\frac{\Delta I}{I_0} \sim \int_{x_1}^{x_2} \frac{1}{N} \frac{\partial N}{\partial y} \, dx, \tag{4}$$

where x is the direction of light propagation through a medium of interest. In schlieren systems, a cutoff such as a knife edge is typically placed after the focusing optic to control the differential amount of refracted light that is recorded. In this way, or equivalently, by adjusting the illumination spot size or focal length of the schlieren head, the proportional constant in Eq. 4 can be tuned such that variable image contrast, sensitivity (the change of contrast with changing refraction angle), and refractive measurement range are all possible. The direction y is normal to the orientation of the optical cutoff. By changing to a vertical or circularly aligned cutoff, the direction of visualizable gradients in refractive index can also be changed.

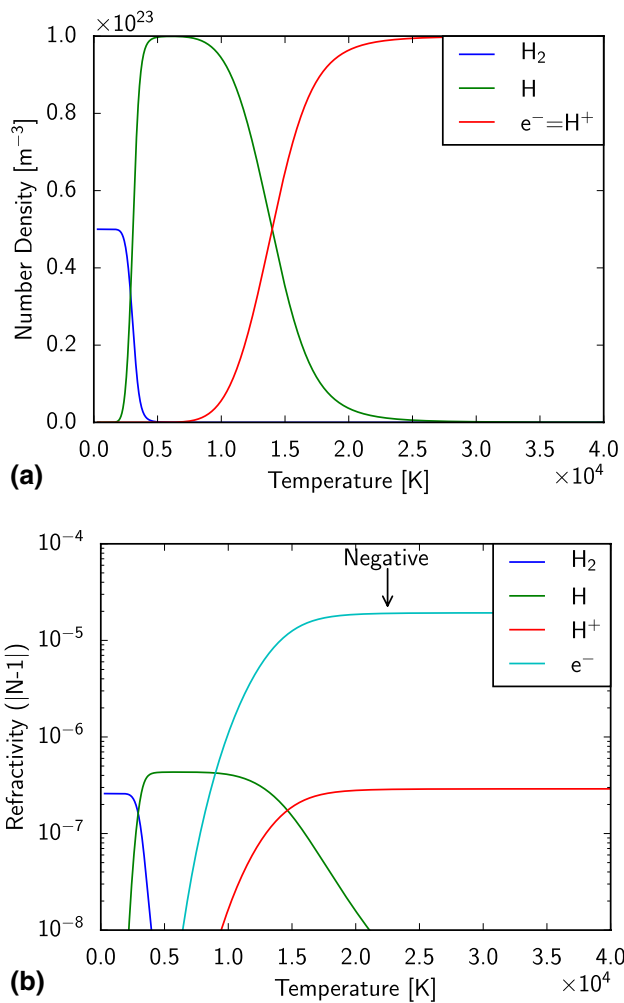A distributed ray tracing illustration showing how a symmetric plasma column distorts a uniform background

source is detailed in Fig. 2. Without any refractive perturbations in the test section, $\partial N/\partial y = 0$ and the schlieren image recorded will follow from the projection of a uniform source onto a camera independent of the amount of light cutoff. When a uniform plasma is added to the test section as in Fig. 2b, rays that traverse the top half of the plasma experience $\partial N/\partial y > 0$ and are bent upward while those on the bottom half experience $\partial N/\partial y < 0$ and are bent downward. By adding a horizontal knife edge at the focus of the optical configuration, the amount of refracted light that is recorded at the camera can be tuned. This results in a recorded image that has a gradient in illuminance proportional to the gradient in refractive index, as described in Eq. 4.

For magnetized plasma jets, the relationship between gradients in recorded intensity and refractive index can be further refined. Specifically for the focus of this work where $T \gg 10^4$ K, contributions to the refractivity from neutral species are negligible. Only in very weakly ionized gases or when visualizing shock phenomena where gradients in neutral density far outweigh charged particle gradients does schlieren selectively visualize neutral particles. Furthermore, as hydromagnetic jets feature characteristic densities and magnetic fields of $n \sim 10^{23}$ m^{-3} and $B \sim 1$ T, respectively, over spatial scales of 0.1-1 cm (Underwood et al. 2017; Subramaniam et al. 2018), gradients in the plasma refractive

index are dominated by gradients in density of free electrons. This allows schlieren to directly visualize the gradients of electron density as gradients in the recorded intensity of background illumination for such flow conditions.

3 Experimental details

The schlieren apparatus used in this study is detailed in Fig. 3. A conventional z-type schlieren configuration with two f/4 60 cm focal length mirrors are employed to eliminate coma and limit astigmatic separation. A $\lambda = 630$ nm, 250 mW continuous wave laser diode is used as a source of background illumination to overwhelm any self-emission emanating from the plasma flow. The output beam of the diode passes through an adjustable focal length, 5 cm lens to expand the beam until it is collimated by the first mirror. The resulting collimated beam then passes through a vacuum test section with quartz crystal windows and is focused by the second mirror onto a series of apertures (baffles) to reject stray light. Near the focus of the second mirror, the beam passes through an optical bandpass filter centered at 635 ± 2 nm with a FWHM of 10 nm to further reject broadband self-emission from the plasma. The beam then passes through an optical cutoff and is recorded with a Shimadzu HPV-X2 camera operating with a continuous sample rate of 10 MHz for 256 consecutive 50 ns exposures.

When a coherent backlight source is used with a conventional knife edge cutoff, geometrical theory begins to break down and diffraction effects become important (Oppenheim et al. 1966). Diffraction can adversely affect the measured image contrast and increase the complexity of interpreting results. To limit these effects, the conventional knife edge cutoff is replaced with a 'sooted' slide that features a sufficiently gradual gradient in cutoff transmission. By changing the cutoff transmission gradient, the tunable features of the schlieren diagnostic discussed in the geometrical limit in Eq. 4 are recovered. The cutoff transmission is controlled by depositing soot onto a glass slide with a flame, as depicted in Fig. 4.

Hydromagnetic plasma jets are created using a pulsed Lorentz force accelerator that is an extension of the classic Marshall plasma gun (Marshall 1960). The device features a coaxial accelerator volume that is 26 cm long, 5 cm in diameter, and includes 0.5 cm diameter rodded anodes and a central copper cathode, as depicted in Fig. 3. A vacuum pressure of 10^{-7} Torr is maintained between successive discharge events to ensure a reliable and consistent discharge process. To initialize a plasma jet, neutral hydrogen gas is introduced into the breach of the accelerator volume using a fast rise-rate, adjustable mass-bit gas puff valve (Loebner et al. 2015b). As the neutral gas propagates into
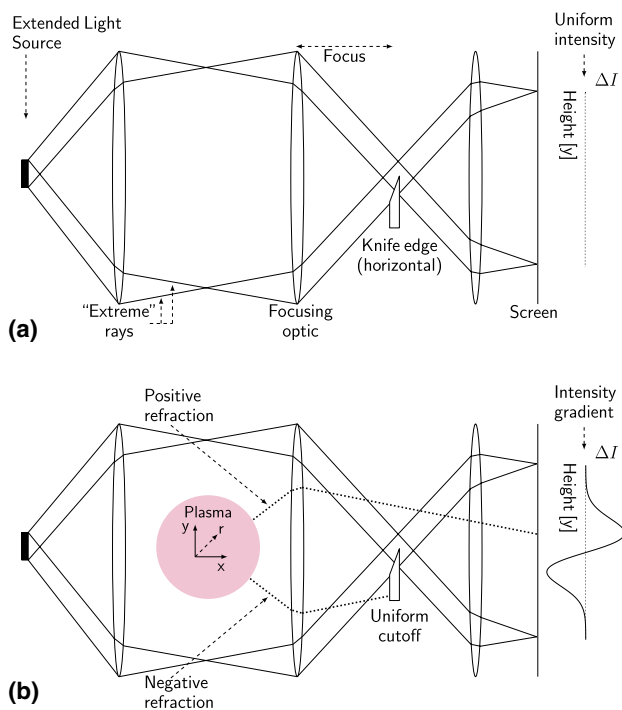

Fig. 2 Distributed ray tracing illustration detailing the effect that a symmetric plasma has on background illumination and how a knife edge can be used to visualize the gradient in plasma refractivity as a gradient in recorded intensity, **a** no plasma, **b** with plasma. Only the 'extreme' rays are visualized
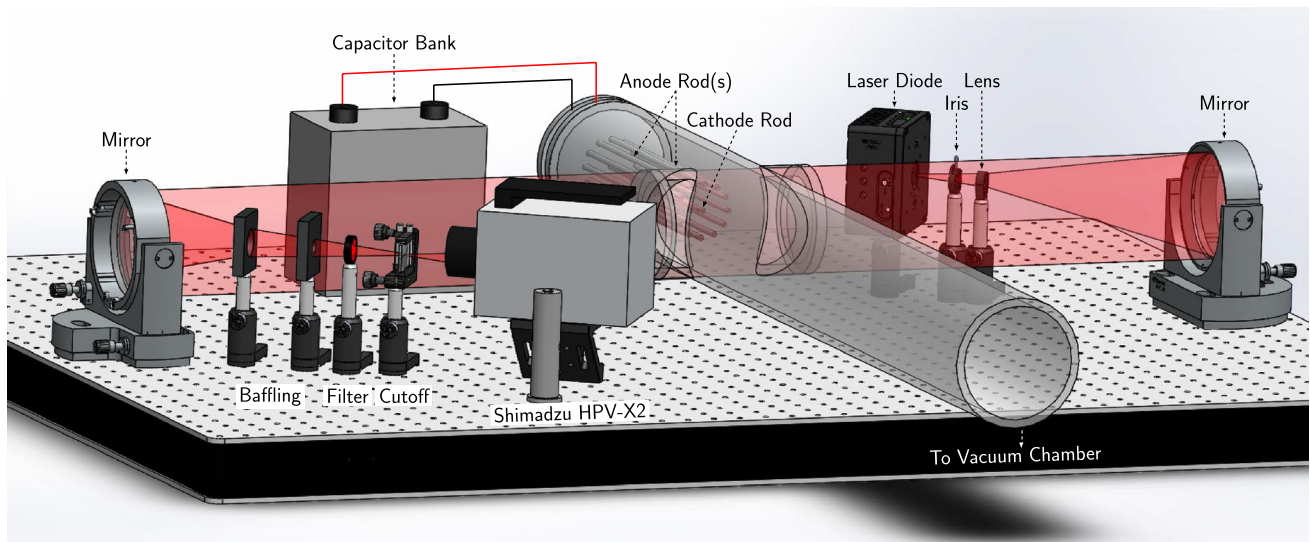
Fig. 3 Experimental schematic of the schlieren apparatus and plasma source used in this study. A z-type schlieren configuration is used with a 630 nm, 250 mW laser backlight source, two $f / 4$ 60 cm focal length mirrors, and a 'sooted' slide as an optical cutoff. Flow dynamics are captured with a Shimadzu HPV-X2 with a continuous sample rate of 10 MHz. The source used to produce plasma jets is a gun device (Marshall 1960)
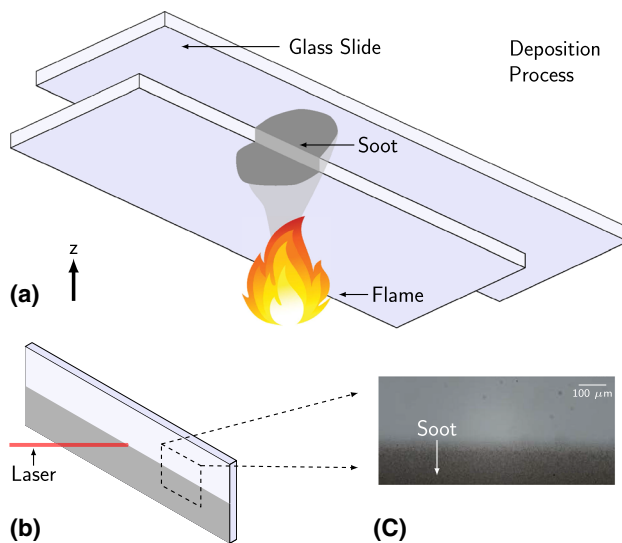

Fig. 4 Details regarding the 'sooted' slide used as an optical cutoff, **a** deposition process, **b** cutoff orientation, and **c** microscope view of soot formation

the accelerator volume, energy is supplied to break down and accelerate the gas up to Alfvénic velocities through a deflagration process that employs an induced axial Lorentz force (Loebner et al. 2015a, 2016b). In this study, a 56 μF capacitor is connected across the electrodes and charged to between 5 and 9 kV with discharge periods lasting up to 10 μs.

3.1 Sensitivity, range, and resolving power

The range of plasma properties over which schlieren methods effectively visualize plasma jets depends on the refraction angle induced by the medium. Assuming an equilibrium plasma column, the refraction angle can be estimated for an axial slice of the jet as a function of characteristic plasma properties. Prior studies have focused on measuring and validating both the structure and viability of Bennett equilibrium models in approximating plasma jets (Subramaniam et al. 2018; Underwood et al. 2017; Loebner et al. 2016a).

To evaluate the refraction angle, a 1 cm diameter plasma column is assumed with the radial electron density and magnetic field profiles specified in Fig. 5. The ion and electron density profiles feature the same amplitude and structure in dense, hydromagnetic jets due to the principle of quasineutrality. However, the contributions to the refractive index and its gradient per ion are orders of magnitude lower than electrons, as shown in Fig. 1b, and thus make a negligible contribution to the refraction angle. Neutral species are not considered in this analysis as they preferentially ionized at high temperatures ($T \gg 10^4 K$). It is assumed that the gradient length scale of plasma properties is much larger than the wavelength of the background illumination. This permits the use of local electromagnetic dispersion relations detailed in Appendix and Section II that do not account for spatial inhomogeneities of the medium itself. Each profile is used to evaluate the local refractive index due to free electrons and is path integrated to evaluate the refraction angle in Eq. 4 as a function of peak electron density, n_0, with $\lambda = 630$ nm.
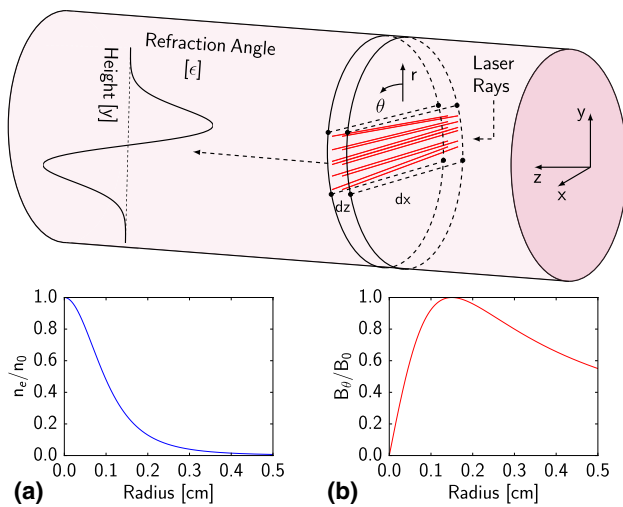
Fig. 5 Equilibrium plasma column model of the jet produced from gun devices, **a** normalized electron density and **b** magnetic field as a function of radius. The ion density profile has the same amplitude and shape as the electron profile due to quasineutrality. Ions contribute negligibly to the index of refraction compared to electrons, as shown in Fig. 1
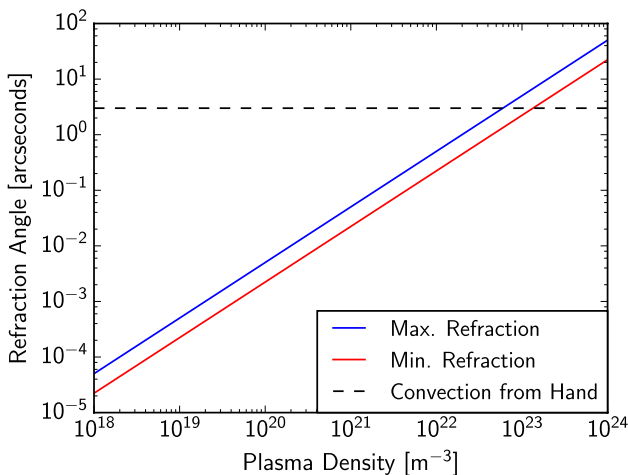

Fig. 6 Refraction angle as a function of the peak electron density in a plasma. The refraction angle evaluated using spatial profiles detailed in Fig. 5. Maximum refraction corresponds to the chord in the plasma column where the maximum deflection occurs. The minimum refraction curve is evaluated at the spatial resolution of the optical system, $y = 0.237$ mm

As detailed in Section II, refractive contributions from the magnetic field are negligible for conditions representative of the Stanford gun facility as $\nabla B \ll \nabla n$.

The result of the refraction angle calculation as a function of peak plasma density is detailed in Fig. 6. As the peak plasma density increases, the corresponding refraction angle of the background illumination also increases. Two specific chords corresponding to the maximum and minimum

deflection of rays propagating through the plasma column are highlighted in Fig. 6. Above $n \sim 10^{22}$ m^{-3}, the region of peak refractive index gradient has a refractive angle of $\epsilon > 2''$, equal to the warm convection from a human hand (Barnes and Bellinger 1945). Threshold values of detectable refraction angles are strongly dependent on both the focusing optics employed and the level of optical cutoff; however, the convection from a human hand is widely regarded as an indicator of high sensitivity (Settles 2012). Closer to the center of the jet, density gradients $\partial N/\partial y \to 0$ and flow features remain unresolvable. The minimum refraction curve in Fig. 6 is evaluated at the spatial resolution of the optical configuration, $y = 0.237$ mm, detailed in Fig. 3. For densities of $n \sim 10^{23}$ m^{-3} previously measured in gun devices, gradients in the plasma profile are resolvable below the spatial resolution of the imaging system with sensitivity greater than established performance metrics of schlieren setups.

Beyond sensitivity, the range of ϵ over which a gradual change of image illuminance occurs is also an important metric of schlieren performance. Figure 6 indicates that for expected densities, a measurement range of 10-100$''$ is more than sufficient to resolve plasma jet flow features. Measurement ranges of this order are common for large diameter, large f/# focusing optics and can be further adjusted in the expense of optical sensitivity by adjusting the amount of cutoff.

Finally, the optical system must have sufficient resolving power or equivalently, resolution, to capture the fine structure present in the plasma flow. This metric is typically quantified in terms of the frequency by which alternating black and white lines can be resolved in the optical system. For the configuration described in Fig. 3, spatial resolution was quantified by printing a rectangular array of black lines on a transparent sheet and placing it in the test section. The spacing between the array of lines was known and used to measure a calibration factor of ~ 0.24 mm/pixel. This corresponds to a minimally resolvable line pair of ~ 0.48 mm and a resolution of approximately 2 line pairs/mm. Resolutions in this range are sufficient to produce sharp schlieren images of plasma jets with characteristic scales ranging from 5-10 mm. Typically limits placed on the optics and alignment for high sensitivity, sufficient measurement range, and uniform cutoff are more restrictive.

3.2 Post-processing

Digital image processing is also used to transform raw schlieren images and further enhance image contrast through a sequence depicted in Fig. 7. Each raw schlieren image first has fixed-pattern artifacts removed by subtracting a background image averaged over the 5–10 frames that are acquired prior to the initiation of each plasma jet. Removing diffraction patterns such as temporally-persistent ring or
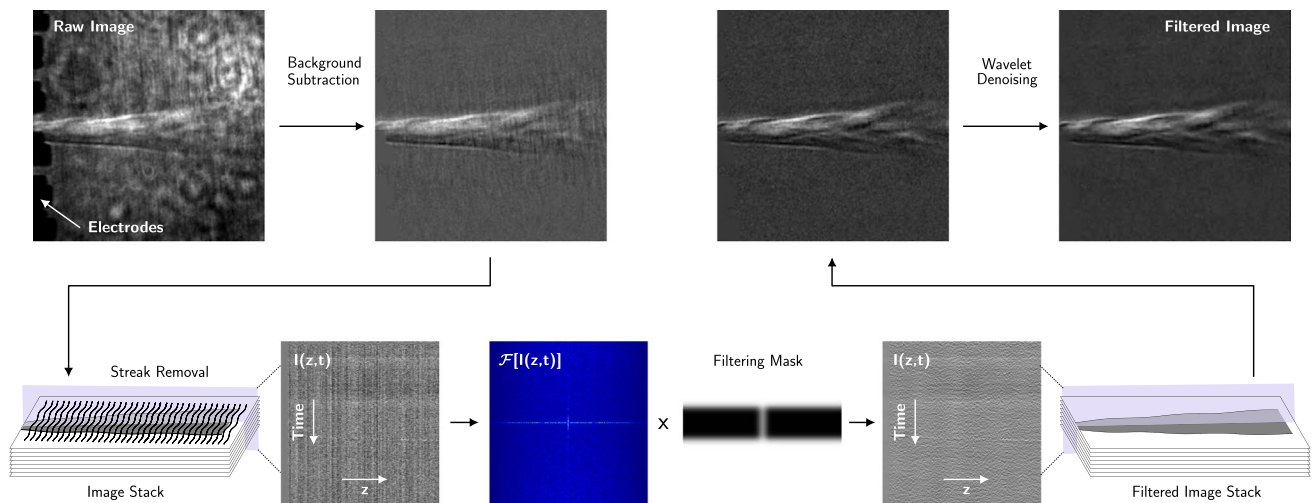
Fig. 7 Post-processing procedure to transform raw schlieren images and improve image contrast

streak artifacts are then processed by taking image slices of the temporal sequence and applying morphological filtering strategies, shown in Fig. 7. In this step, individual slices of the z-t plane are taken and two-dimensional discrete Fourier transforms are computed. A filtering mask is then applied to selectively remove temporally persistent features near the horizontal axis in the transformed image. The image is then regenerated from the filtered Fourier domain by performing an inverse discrete transform. This process is repeated and performed on each z-t slice of the schlieren image stack. Finally, a wavelet thresholding method is employed to further reduce the appearance of sensor noise in final images. Additional details regarding the filtering steps can be found in (Loebner 2017).

4 Experimental results

4.1 Comparison between schlieren and broadband emission

A vertical slice of visualizations using both schlieren imaging and broadband emission for two separate discharge events is detailed in Fig. 9. The broadband intensity measurements were taken by removing the laser schlieren backlight and recording the self-emission from the plasma integrated over the visible spectrum. The image slices are taken 1 cm downstream of the outer anodes after 3.5 μs of the 2.3 kJ discharge pulse. As predicted in Section II, the measured schlieren intensity distribution features values both above and below background levels, ΔI, within the observed plasma jet profile. This characteristic gradient follows from Eq. 4 and is a direct visualization of gradients in plasma density. Self-emission on the other hand features an

intensity profile that peaks on the center axis and decreases with increasing height. Unlike schlieren, interpreting the emission and attributing it to individual flow properties or species is a difficult task. Contributions to intensity from free–free, free-bound, and bound–bound transitions mean that signal levels are a strong function of flow temperature, flow composition, and plasma density.

Although emission offers high levels of signal when visualizing plasma flows, it fails to offer the sensitivity and tunability of schlieren. These features allow schlieren to selectively observe small scale perturbations that would otherwise be buried in the noise of hot, dense jets. For instance in Figs. 8, 9, emission is unable to resolve flow perturbations in the plasma jet profile due to the high levels of signal near the center of the jet. Over the lifetime of the jet, this means that visualizations via emission are unable to capture the same level of detail necessary to identify the growth of unstable flow features. This is illustrated in Fig. 8 where visualizations made with schlieren more clearly resolve small scale features of the plasma jet over its evolution during the 10 μs discharge pulse.

4.2 Plasma jet dynamics

The schlieren apparatus described in Fig. 3 permits novel visualizations of hydromagnetic systems that are simultaneously capable of resolving both characteristic Alfvénic timescales, $\tau_{\mathrm{Alf}} \sim r/V_{\mathrm{Alf}} \sim 100$ ns, and spatial flow features. Importantly, the apparatus allows visualizations to continue in a cinematic manner with exposure times of 50 ns and a sample rate of 10 MHz over the duration of the jet's lifetime. This enables detailed understanding regarding the evolution of both flow structure and stability in hydromagnetic systems.
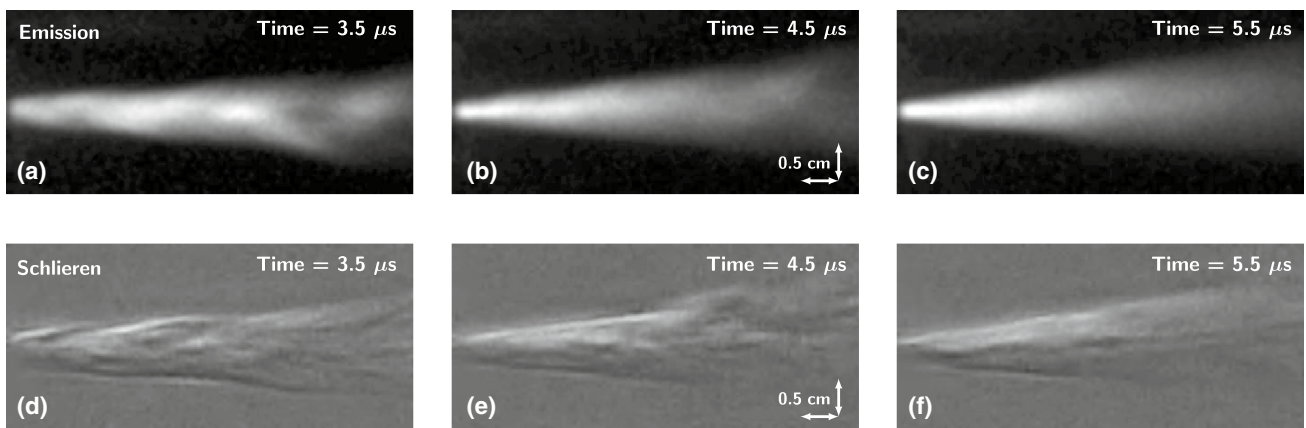
Fig. 8 Visualization made using broadband emission (**a–c**) and schlieren (**d**, **f**), at select times of a 2.3 kJ discharge pulse
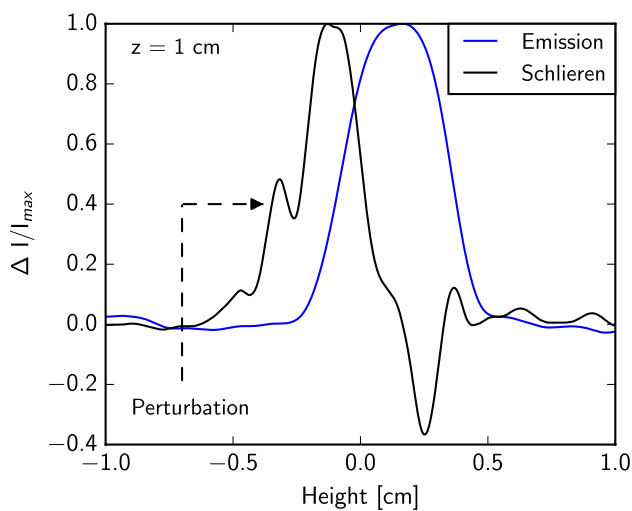

Fig. 9 Normalized levels of intensity above or below background levels, $\Delta I/I_{max}$, as a function of height using both schlieren and self-emission. Vertical slices are taken 1 cm downstream after 3.5 µs of a 2.3 kJ discharge

The temporal variation of the jet diameter is detailed in Fig. 10 for different charging energies at an axial distance 0.85 cm downstream of the accelerator electrodes. It was observed that with increasing drive current, the observed jet diameter decreases. This is consistent with theories that predict the induced magnetic field, and thus drive current play an important role in determining flow structure through an imposed magnetic pressure (Underwood et al. 2017). Similar analyses can be performed at any axial location to uncover details about the manner in which current flows and influences structural patterns within the jet. Dynamic perturbations in the size of the jet are also visible in Fig. 10 after the run down period needed to accelerate the plasma out of the gun volume. The frequency and amplitude of oscillations in the jet size were observed to reduce until jet breakup occurs
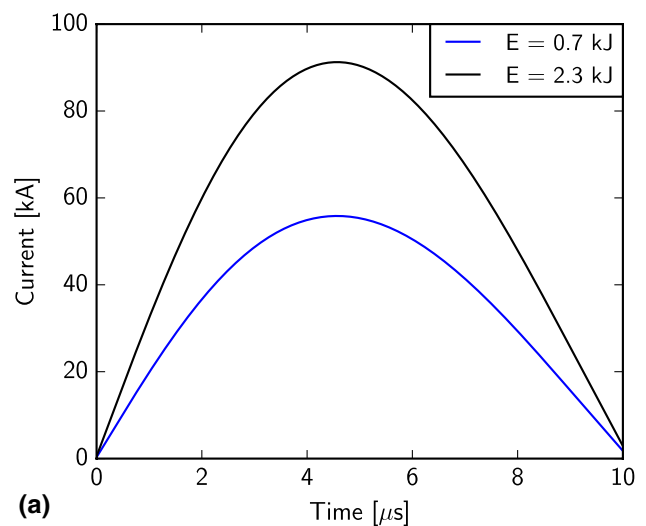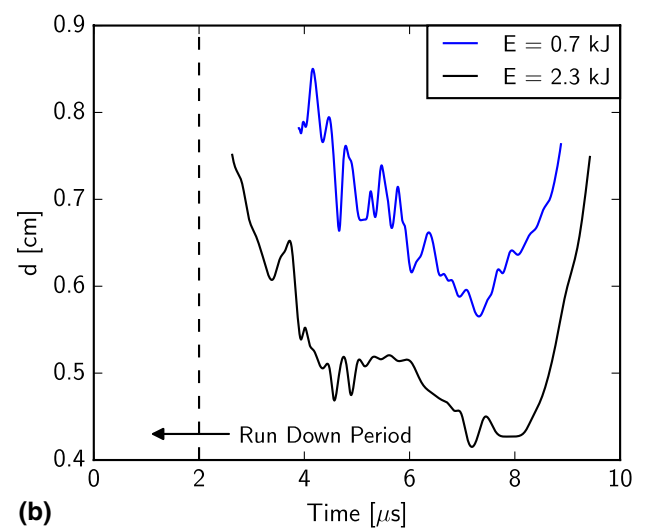
Fig. 10 **a** Current pulses and **b** jet diameter, d, as a function of time and charging energy. The diameter measurements are taken 0.85 cm downstream of the electrodes
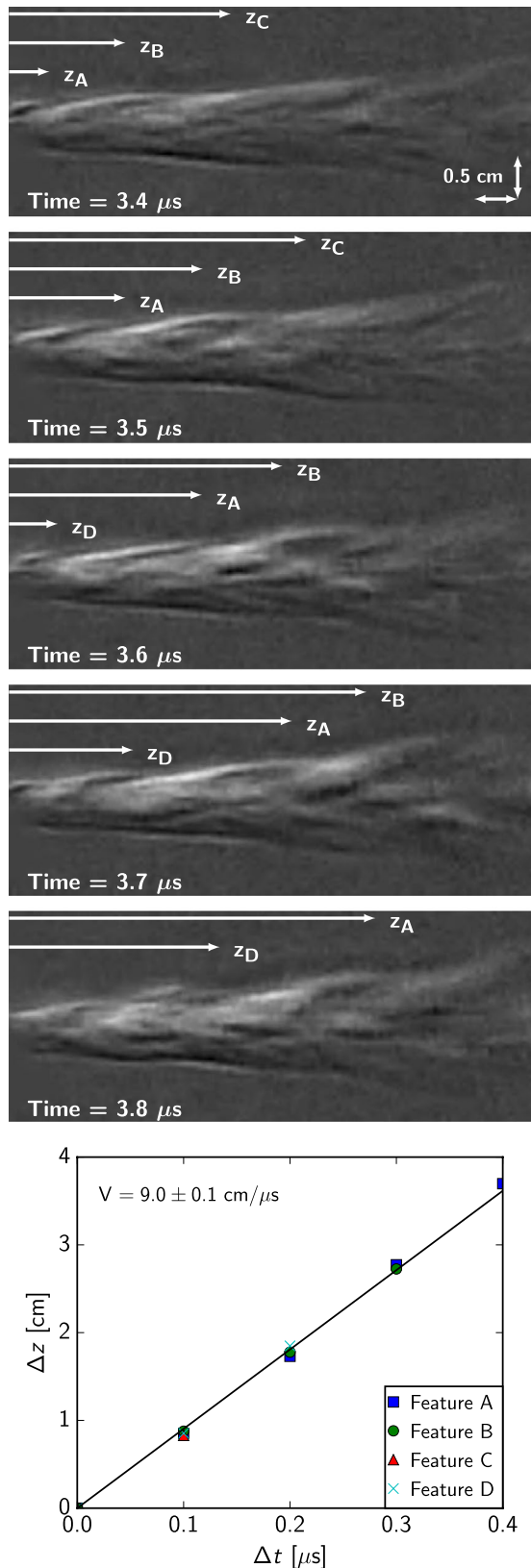
Fig. 11 Coherent features are labeled and tracked over a 0.4 μs interval. A phase velocity of 9.0 ± 0.1 cm/μs (90 ± 1 km/s)

when current levels are insufficient to further conduct and accelerate neutral gas. This indicates plasma jets undergo a transition to smooth and quasi-steady operation as the flow is established.

The evolution of identified and tracked coherent flow features are detailed in Fig. 11 for a charging energy of 2.3 kJ. As the jet forms, perturbations in the plasma column are present that resemble classical magnetohydrodynamic instability modes. Later in the current pulse, the perturbations disappear as the observed oscillations in the jet size, depicted in Fig. 10, also reduce in amplitude and frequency. To quantify the perturbations, 4 different features, A–D, are tracked as they convect downstream over a span ranging 0.4 μs. Using this information, an average phase velocity of $V \sim 9.0 \pm 0.1$ cm/μs (90 ± 1 km/s) was measured. Importantly, the schlieren diagnostic has allowed a novel visualization of plasma jets that demonstrate their formation is a dynamic process that includes the creation of small scale flow features.

4.3 Bow shock dynamics

To study the interaction between plasma jets and magnetized bodies in the laboratory, a 0.48 cm diameter, 1.3 T SmCo magnet was placed 4.2 cm downstream of the accelerator volume. The magnet was oriented to mimic the dipole field experienced by the solar wind as it impinges on Earth. A plasma jet was stagnated against the magnet to initiate the formation of a bow shock, as visualized in Fig. 12 at select times. Given high levels of recombination radiation present in stagnating flows at target interfaces, refraction techniques such as schlieren are well suited at resolving the detached shock boundary. In Fig. 12, schlieren clearly captures the existence of an extended bow shock structure offset from the center of the magnet. Interestingly, dynamic variations in the shock profile are also observed during the stagnation process.

Horizontal and vertical slices of the bow shock are arranged into streak images in Fig. 13. Slices measure the shock standoff distance relative to the magnet centerline and apex for horizontal and vertical streaks respectively. The periodic fluctuations in the shock boundary observed in Fig. 12 are also seen in each of the streak images. The periodicity in Fig. 13 indicates that the shock boundary oscillations decrease in frequency from 4 MHz near 6 μs to less than 1 MHz near the end of the discharge. The structure and timescale of fluctuations in the bow shock indicate that coherent features in the stagnating plasma jet couple to the bow shock and dynamically influence its standoff distance.
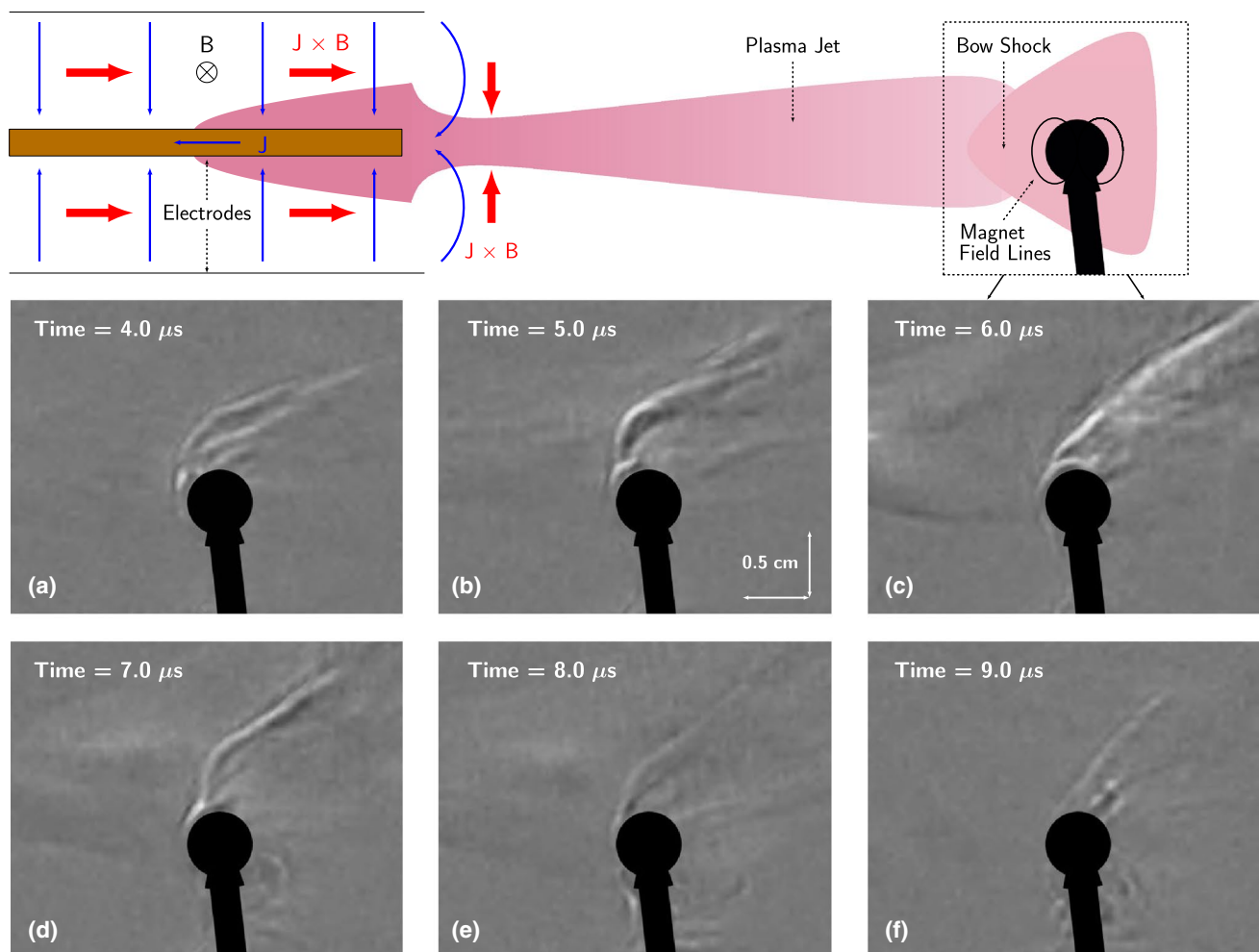
Fig. 12 Bow shock dynamics around a 0.48 cm diameter, 1.3 T SmCo magnet. The target was placed 4.2 cm downstream of the accelerator volume. The shock forms as a result of plasma jet stagnation generated with a charging energy of 1 kJ

5 Conclusions

In this work, we have described a novel schlieren apparatus and used it to visualize the dynamics of hydromagnetic systems. An expansive discussion of both the underlying theory and features of the diagnostic is included to characterize its ability to visualize plasma flows. A detailed image processing procedure is introduced that further rejects diffractive schlieren artifacts and produces the image contrast needed to visualize plasma flows. Images captured using conventional broadband self-emission are included to aid in the interpretation of the schlieren signal and illustrate its tunable sensitivity. Importantly, the schlieren diagnostic has the ability to simultaneously resolve both Alfvénic timescales and spatial flow features of interest in a cinematic manner.

We use the diagnostic to capture the dynamics of plasma jet formation and stagnation. The development of coherent flow structures is observed indicating that the transition to quasi-steady flow is a dynamic process. Finally, by visualizing the stagnation of plasma jets on magnetized targets, the process by which these coherent features translate into perturbations of magnetized bow shocks is observed. This study of the formation dynamics of magnetized bow shocks is an important phenomena in many astrophysical settings. On Earth, the existence of a bow shock enables the planet to support life by shielding its surface from the harmful effects of the solar wind. However, given the scales of interest, systemic studies in space that capture the dynamic interaction between plasma and resulting shock formation are not possible. This necessitates further study of laboratory astrophysics and plasma systems alike with high bandwidth and spatially resolved diagnostics such as detailed in this work.
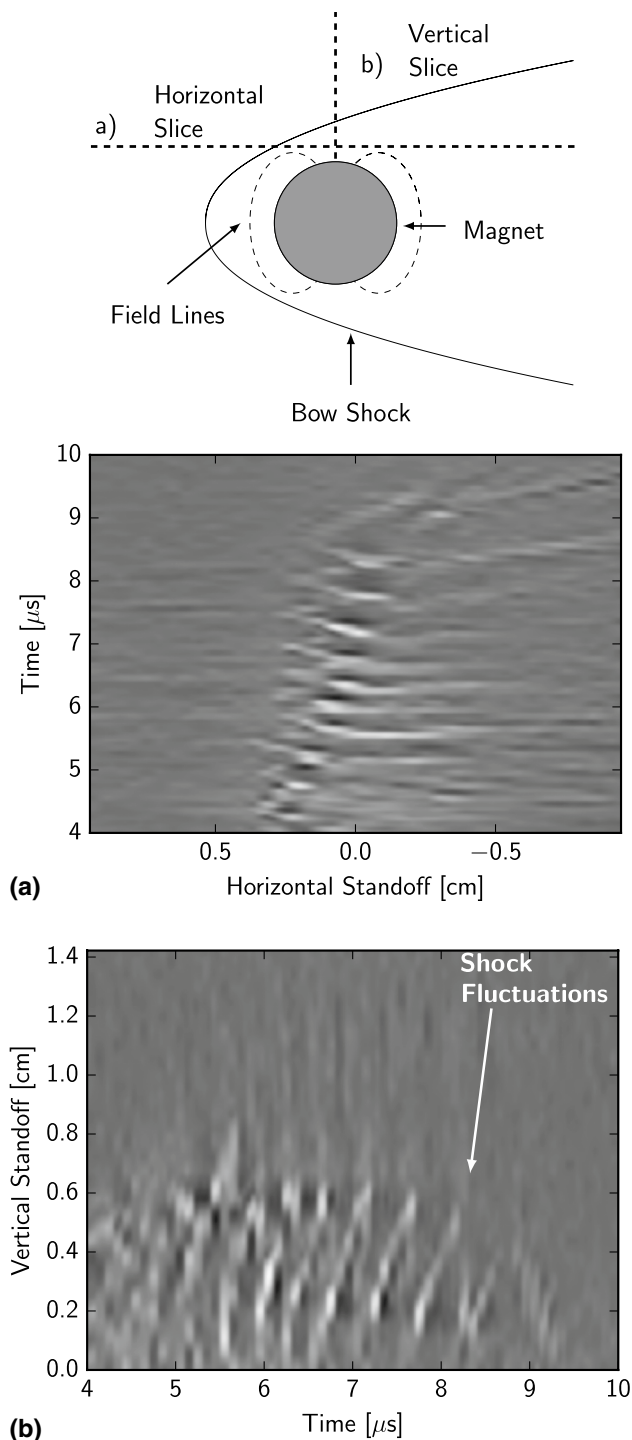
(a)

(b)

Fig. 13 a Horizontal and **b** vertical slices of the magnetized bow shock visualized in Fig. 12. Shock fluctuations are observed with decreasing frequency as the stagnating plasma jet evolves

Appendix: Appleton–Hartree equation

This equation describes the refractive index for electromagnetic wave propagation, N_e, in a magnetized, collisionless plasma according to,

$$N_e^2 = 1 - \frac{X}{Z}$$

$$Z = 1 - \frac{Y^2 \sin^2 \theta}{2(1-X)} \pm \frac{1}{1-X} \left(\frac{1}{4} Y^4 \sin^4 \theta + \cdots \right.$$

$$\left. Y^2 \cos^2 \theta (1-X)^2 \right)^{1/2}, \tag{5}$$

where θ is the angle between the magnetic field vector and the wave propagation vector, $X = \omega_p^2/\omega^2$, and $Y = \omega_H/\omega$. In these expressions, $\omega_p = \sqrt{n_e e^2/\epsilon_0 m_e}$ is the electron plasma frequency and $\omega_H = B_0 |e|/m_e$ is the electron cyclotron frequency. From these expressions, the term $K'_e(n_e, B)$ that appears in Eq. 1 can be evaluated directly,

$$K'_e(n_e, B) = \sqrt{1 - \frac{X}{Z}} - 1. \tag{6}$$

References

Alpher RA, White DR (1959) Optical refractivity of high-temperature gases. II. Effects resulting from ionization of monatomic gases. Phys Fluids 2(2):162–169. https://doi.org/10.1063/1.1705907

Barnes NF, Bellinger SL (1945) Schlieren and shadowgraph equipment for air flow analysis. JOSA 35(8):497–509

Bickerton R (1980) Pinch research. Nuclear Fusion 20(9):1072

Cassibry JT, Thio YCF, Wu ST (2006) Two-dimensional axisymmetric magnetohydrodynamic analysis of blow-by in a coaxial plasma accelerator. Phys Plasmas 13(5):053101. https://doi.org/10.1063/1.2196245

Cassibry JT, Cortez RJ, Hsu SC, Witherspoon FD (2009) Estimates of confinement time and energy gain for plasma liner driven magnetoinertial fusion using an analytic self-similar converging shock model. Phys Plasmas 16(11):112707. https://doi.org/10.1063/1.3257920

Cheng DY (1970) Plasma deflagration and the properties of a coaxial plasma deflagration gun. Nuclear Fusion 10(3):305

Gladstone JH, Dale TP (1863) XIV. Researches on the refraction, dispersion, and sensitiveness of liquids. Philos Trans R Soc Lond 153:317–343

Hassani-Gangaraj M, Veysset D, Nelson KA, Schuh CA (2018) Melt-driven erosion in microparticle impact. Nat Commun 9(1):5077. https://doi.org/10.1038/s41467-018-07509-y

Kalantar DH, Hammer DA (1993) Observation of a stable dense core within an unstable coronal plasma in wire-initiated dense z-pinch experiments. Phys Rev Lett 71:3806–3809. https://doi.org/10.1103/PhysRevLett.71.3806

Loebner KTK (2017) Physics and applications of a plasma deflagration accelerator. PhD thesis, Stanford University

Loebner KTK, Underwood TC, Cappelli MA (2015a) Evidence of branching phenomena in current-driven ionization waves. Phys Rev Lett 115:175001. https://doi.org/10.1103/PhysRevLett.115.175001

Loebner KTK, Underwood TC, Cappelli MA (2015b) A fast rise-rate, adjustable-mass-bit gas puff valve for energetic pulsed plasma experiments. Rev Sci Instrum 86(6):063503. https://doi.org/10.1063/1.4922522

Loebner KTK, Underwood TC, Mouratidis T, Cappelli MA (2016a) Radial magnetic compression in the expelled jet of a plasma deflagration accelerator. Appl Phys Lett 108(9):094104. https://doi.org/10.1063/1.4943370

Loebner KTK, Underwood TC, Wang BC, Cappelli MA (2016b) Damage morphologies in targets exposed to a new plasma deflagration accelerator for elm simulation. IEEE Trans Plasma Sci 44(9):1534–1540. https://doi.org/10.1109/TPS.2016.2565508

Marshall J (1960) Performance of a hydromagnetic plasma gun. Phys Fluids 3(1):134–135. https://doi.org/10.1063/1.1705989

Merzkirch W (2012) Flow visualization. Academic Press, Cambridge

Mitchner M, Kruger C (1992) Partially Ionized gases. Wiley, Hoboken

Nakajima A, Uchida G, Kawasaki T, Koga K, Sarinont T, Amano T, Takenaka K, Shiratani M, Setsuhara Y (2015) Effects of gas flow on oxidation reaction in liquid induced by He/O2 plasma-jet irradiation. J Appl Phys 118(4):043301. https://doi.org/10.1063/1.4927217

Oppenheim AK, Urtiew PA, Weinberg FJ, Gaydon AG (1966) On the use of laser light sources in schlieren-interferometer systems. Proc R Soc Lond Series A Math Phys Sci 291(1425):279–290. https://doi.org/10.1098/rspa.1966.0095

Patek SN, Caldwell RL (2005) Extreme impact and cavitation forces of a biological hammer: strike forces of the peacock mantis shrimp odontodactylus scyllarus. J Exp Biol 208(19):3655–3664. https://doi.org/10.1242/jeb.01831, http://jeb.biologists.org/content/208/19/3655.full.pdf

Settles GS (2012) Schlieren and shadowgraph techniques: visualizing phenomena in transparent media. Springer, Berlin

Shumlak U, Golingo RP, Nelson BA, Den Hartog DJ (2001) Evidence of stabilization in the Z-pinch. Phys Rev Lett 87:205005. https://doi.org/10.1103/PhysRevLett.87.205005

Subramaniam V, Underwood TC, Raja LL, Cappelli MA (2018) Computational and experimental investigation of plasma deflagration jets and detonation shocks in coaxial plasma accelerators. Plasma Sour Sci Technol 27(2):025016

Thio YCF (2008) Status of the US program in magneto-inertial fusion. J Phys Conf Ser 112(4):042084

Underwood TC, Loebner KT, Cappelli MA (2017) A plasma deflagration accelerator as a platform for laboratory astrophysics. High Energy Density Phys 23:73–80. https://doi.org/10.1016/j.hedp.2017.03.004

White DR (1961) Optical refractivity of high-temperature gases. III. The hydroxyl radical. Phys Fluids 4(1):40–45. https://doi.org/10.1063/1.1706187